Optical Phase Measurements of Disorder Strength Link Microstructure to Cell Stiffness

4 authors, including:

Zachary Steelman
Duke University
40 PUBLICATIONS   **393** CITATIONS

SEE PROFILE

Adam Wax
Duke University
356 PUBLICATIONS   **6,699** CITATIONS

SEE PROFILE

Some of the authors of this publication are also working on these related projects:

Coherent Light Microscopy: Imaging and Quantitative Phase Analysis a cura di Pietro Ferraro,Adam Wax,Zeev Zalevsky View project

Advanced functional OCT View project

Optical Phase Measurements of Disorder Strength Link Microstructure to Cell Stiffness

Will J. Eldridge,[1] Zachary A. Steelman,[1] Brianna Loomis,[1] and Adam Wax[1,*]
[1]Duke University, Department of Biomedical Engineering, Durham, North Carolina

ABSTRACT   There have been sustained efforts on the part of cell biologists to understand the mechanisms by which cells respond to mechanical stimuli. To this end, many rheological tools have been developed to characterize cellular stiffness. However, measurement of cellular viscoelastic properties has been limited in scope by the nature of most microrheological methods, which require direct mechanical contact, applied at the single-cell level. In this article, we describe, to our knowledge, a new analysis approach for quantitative phase imaging that relates refractive index variance to disorder strength, a parameter that is linked to cell stiffness. Significantly, both disorder strength and cell stiffness are measured with the same phase imaging system, presenting a unique alternative for label-free, noncontact, single-shot imaging of cellular rheologic properties. To demonstrate the potential applicability of the technique, we measure phase disorder strength and shear stiffness across five cellular populations with varying mechanical properties and demonstrate an inverse relationship between these two parameters. The existence of this relationship suggests that predictions of cell mechanical properties can be obtained from examining the disorder strength of cell structure using this, to our knowledge, novel, noncontact technique.

INTRODUCTION

Cellular mechanical properties are of interest across many fields of inquiry as these attributes can illuminate cellular processes, distinguish cell phenotypes, uncover disease origins, and point the way toward new therapeutic strategies. The typical mode of investigating these properties is to measure the viscoelastic parameters that describe a cell's mechanical features and examine how they are modulated due to cellular phenomena (1–4). Cellular phenotype has shown to be a strong modulator of cellular stiffness, which consequently affects cellular physiology and behavior (2,5–8). Cell mechanical properties are also important for cancer biology, because cellular stiffness in tumors has been shown to differ significantly from that of the surrounding tissue, partially due to abnormal behavior of the cytoskeleton (9–11). Further, changes in cancer cell mechanics also greatly impact the ability of these cells to withstand chemotherapy and metastasize (12). To generate metastatic sites, tumor cells must detach from the primary tumor and migrate through the extracellular matrix to reach the vasculature and travel to a secondary location (13). Modification of mechanical features enables increased cell motility,

which has been shown to promote progression of cancer in many studies (14). Therefore, detecting modulation in cellular stiffness in cancer could be used as an early sign of oncogenesis.

Many experimental techniques have been developed to quantify mechanical properties of biological cells. The most commonly used modality to measure cellular stiffness is atomic force microscopy, which indents the cellular surface with a micron-sized bead attached to a cantilever while the motion of the cantilever is monitored by an optical sensor (5,6,8–11,15,16). Other methods have also been employed, including indentation using an optically trapped bead (16), and micropipette aspiration (17), where suction is used to draw a cell into a confined space while tracking its surface displacement. However, all of these methods require complex schemes and alignment procedures, and significantly, are inherently invasive, in that each applies a force via an element that is exogenous to the typical cellular microenvironment. Micropillar substrates have recently been used to visualize actin-ordering and modulation of cellular viscoelasticity due to changes in substrate stiffness (18). However, fabrication of such substrates with tightly controlled properties can be difficult and the data require detailed image analysis to obtain mechanical information. To address this limitation, we have recently created a novel assay that uses quantitative phase imaging (QPI) to track

CrossMark

displacement of cells due to shear flow to assess cell stiffness (19). QPI has been widely applied to cell imaging of dynamic processes (20–23), especially for examining red blood cell membrane fluctuations (24–27). The nanoscale sensitivity of QPI enables detection of subtle mass displacement in response to application of stimuli, such as shear stress. In our assay, the use of shear stress avoids the need for cell manipulation, permitting higher throughput measurements and simplified analysis.

Access to nanoscale information has provided new avenues for cell biology studies (28–31). For example, early carcinogenesis is marked by alterations in the nanoarchitecture of cellular morphology that are not apparent with conventional microscopy and histopathology (32,33). Recently, partial wave spectroscopy (PWS) has been developed to probe nanoscale structural changes in early carcinogenesis. In PWS, spectral reflectance data are analyzed to assess a metric termed "disorder strength" (L_D) that describes the degree of structural heterogeneity (32–36). The utility of disorder strength was initially shown by discriminating between two cell lines that were found to be similar upon histopathological analysis, but which have differing malignant aggressiveness (33), with the more aggressive cells presenting substantially larger disorder strength. Further studies using PWS attributed these changes to cytoskeletal composition by examining modulation of L_D due to treatment with cytoskeletal disrupting toxins (32). Measurements of disorder strength have also been employed in clinical studies to distinguish cytologically normal pancreatic cells from healthy patients and cytologically malignant pancreatic cells from cancer patients, possibly suggesting a new avenue for pancreatic cancer diagnosis (35). PWS has also been used to identify changes in nanoscale cellular architecture from normal-appearing cells taken from tissue locations remote from the primary tumor site. This concept of "field carcinogenesis" has been used to assess risk of colon cancer from visually normal rectal tissue (34) by using PWS to analyze these histologically unapparent nanoscale changes in cellular morphology.

In this article, we propose a new method for measuring disorder strength based on analysis of quantitative phase images. The simplified scheme of this approach permits analysis across a substantial number of individual, live cancer cells. Significantly, we show that phase-based measurements of disorder strength correlate highly with mechanical stiffness parameters across cell populations, suggesting a fundamental relationship between these two cell descriptors. It is reasonable to hypothesize that a relationship between phase disorder strength and cellular stiffness should exist, given previous results that relate disorder strength to structural changes usually associated with modulation of cellular stiffness (32). Further, another recent study has shown that increased cytoskeletal organization, corresponding to lower disorder, results in an increased ability of cells to generate traction forces, a measure of their mechanical properties (18). To support this hypothesis, we analyzed the disorder strength and cell stiffness of three different cell lines: HT-29 colon cancer cells, A431 skin cancer cells, and A549 lung cancer cells. In addition to these three, cells with transformed mechanical properties were also examined, including HT-29 cells with a C-terminal Src kinase (CSK) knockdown and A431 cells that were pharmacologically disrupted with cytochalasin D, a fungal actin depolymerizing toxin. The correspondence between the changes in structure and mechanical properties is discussed both as a potential means for high throughput measurements of cellular mechanical properties and for implications as a scaling law.

MATERIALS AND METHODS

QPI system

The QPI instrument (Fig. 1), was designed to perform quantitative phase spectroscopy over the visible range (37) by implementing a rapidly tunable optical source with a large enough bandwidth to reduce speckle in these coherent optical measurements. This system has been used previously to visualize cellular dynamics in a variety of experiments, including examination of red blood cell membrane fluctuations (27) and cardiomyocyte contractions (23). Collimated white light from a single-mode supercontinuum source (Fianium, Southampton, UK) was passed through a holographic diffraction grating (300 lp/mm) to spatially separate wavelengths. A galvanometric scanning mirror and 10× objective (Carl Zeiss, Oberkochen, Germany) were used to couple selected wavelengths from the spectrally separated light into a single-mode fiber. For these studies a center wavelength and full-width-half-maximum of 589 and 1.2 nm, respectively, were used, which corresponds to a coherence length of 167 μm, calculated using the standard form used in optical coherence tomography (38). This coherence length ensures that interferometric efficiency is not compromised across the field of view, while serving to reduce coherent artifacts. The light in the single mode fiber passes through a linear polarizer before being introduced to the QPI system, which is implemented as an off-axis Mach-Zehnder configuration. Path-length matching stages in both arms were used to balance the optical path length after introduction of the sample. Light from both arms was collected using matched microscope Plan-NeoFLUAR 40×, 0.75 NA objectives (Carl Zeiss) that was projected onto a fast CMOS camera (Photron, Tokyo, Japan) with an effective magnification of 107× (corresponding to a final pixel size of 0.18 μm). The spatial phase noise of the system was measured to be 8×10^{-3} rad.

Image processing for phase retrieval

Images were processed digitally using previously described methods (19,37,39). Combination of the sample beam with an off-axis reference beam introduces a spatial interferometric fringe in the image that contains information regarding the complex sample field. Using custom MATLAB (The MathWorks, Natick, MA) code, Fourier-transforming the interferogram separates the background sample and reference intensities from the off-axis terms of interest, which are then isolated via a spatial filter. The retrieved complex field was digitally refocused via the Fresnel kernel to the expected focal plane using an automated algorithm (39). After refocusing, the phase profile was calculated and unwrapped to remove 2π ambiguities. Lastly, the background phase field was fit to a low-order polynomial
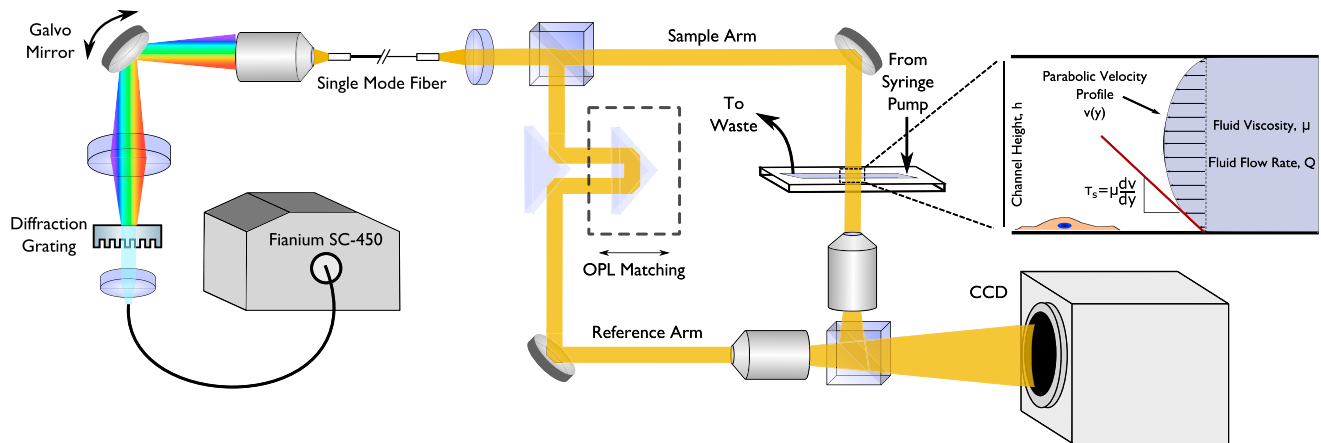
FIGURE 1 Diagram of quantitative phase imaging instrument. Light from a supercontinuum source is spectrally filtered using a diffraction grating to obtain low coherence illumination ($\lambda = 589 \pm 1.2$ nm, corresponding to a coherence length of 167 μm). Light passes through the sample of interest before being combined with a reference beam and projected onto a fast charge-coupled device camera. (*Top-right inset*) Flow channel with the presumed parabolic flow. The channel geometry and fluid properties define the expected shear stress on the cells of interest (see Materials and Methods for more information). To see this figure in color, go online.

and subtracted from the final image to reveal the detrended cell-induced phase profile.

Calculation of disorder strength

Disorder strength was evaluated from quantitative phase images of cells obtained before the onset of shear flow. Each cell image is masked using a phase threshold level >1.75 rad and fit to a low-order (fifth) polynomial. This threshold was chosen to avoid edge effects at the edge of cells. The polynomial was subtracted from the phase image to isolate the fluctuating component of the phase data such that the overall trend of a slowly increasing phase toward the cellular apex is removed. The variance of the phase, $\langle \Delta\varphi(x,y)^2 \rangle$ is calculated from the detrended data in the $3{\times}3$-pixel neighborhood surrounding each point (x,y) using custom MATLAB code. In calculating the average variance for each cell, the data were further thresholded at phase values >2.75 rad to provide comparable areas of interrogation for each of the cells lines, so that differences in area did not confound phase disorder strength calculations. Only the A431-CD cells had a significantly different area of interrogation after this threshold was applied.

Calculation of effective shear stiffness

Effective shear stiffness constants, k_s, were calculated using the methods described in Eldridge et al. (19). Once cells were plated in a flow chamber, the chamber was securely attached to the sample stage and connected to a syringe pump. Based on a parallel plate geometry and the no-slip boundary condition, the shear stress at the cell adhesion surface is calculated to be $\tau = 6\mu Q/Wh^2$, where μ is the dynamic viscosity of the culture media (assumed to be the same as water at room temperature), Q is the volumetric flow rate, W is the width of the flow channel, and h is the height of the flow channel (40). The value Q was selected to provide a shear stress of ~8 dyne/cm^2, which was sufficient to perturb the cells yet not dislodge them from the substrate. Cells were imaged for 2 s with no flow, followed by a step increase in shear stress to the aforementioned value for 8 s. Cell images were captured at 60 or 125 frames per second. Assuming a homogeneous medium, the movement of the center of mass (COM) can be calculated by analyzing the phase displacement over the course of the stress. The mass, m, at a given pixel can be calculated as $m = 2\pi \Delta n\, d(x,y)\, A_{\mathrm{pixel}}/\alpha$, where α, the refractive index (RI) increment, is defined as the change in RI per concentration unit and A_{pixel} is the area of the pixel. Dependence on α and Δn is cancelled when calculating COM such that (19):

$$\vec{r}_{\mathrm{COM}}(t) = \frac{\sum_i \varphi(x_i, y_i) x_i}{\sum \varphi(x,y)}\widehat{x} + \frac{\sum_i \varphi(x_i, y_i) y_i}{\sum \varphi(x,y)}\widehat{y}$$
$$+ \frac{\sum_i \varphi(x_i, y_i) z_i}{\sum \varphi(x,y)}\widehat{z},$$
(1)
$$\vec{r}_{\mathrm{COM}}(t) = \Delta x_{\mathrm{COM}}\widehat{x} + \Delta y_{\mathrm{COM}}\widehat{y} + \Delta z_{\mathrm{COM}}\widehat{z},$$

where r_{COM} and Δx_{COM}, Δy_{COM}, and Δz_{COM} are the total COM vector and directional COM locations over time, respectively. The COM displacement was referenced to its initial location before shear flow (i.e., $t = 0$). A more detailed discussion of the COM measurement and factors that impact its determination may be found in Eldridge et al. (19). The effective force on the cell was calculated by multiplying the shear stress by the projected surface area, SA_{cell} (assuming a RI difference of 0.04, which was found to be a valid assumption based on our prior measurements (19)), such that $F = \tau \times SA_{\mathrm{cell}}$. The total COM deviation was then fit to a one-dimensional (1D) Kelvin-Voigt model of stiffness so that cellular mechanical properties to be described by a stiffness (k_s, N/m) and damping element (η, Ns/m) (19) can be written:

$$\left| \vec{r}_{\mathrm{COM}}(t) \right| = \frac{F}{k_s}\left(1 - e^{-tk_s/\eta}\right).$$
(2)

While the shear stress does decrease axially along the height of the cell due to the parabolic flow within the chamber, laminar flow equations for rectangular ducts suggest that the shear stress would not vary substantially at heights typical for cells (19,41).

Cell culture and flow cell platform

HT-29 colon cancer cells and HT-29 cells with CSK shRNA-mediated knockdown were cultured using McCoy's 5A medium + 10% fetal bovine serum + 1 μL/mL of Pen-Strep antibiotic. CSK cells were additionally supplied 20 μL/mL of geneticin as a selective antibiotic. A431 skin cancer cells were cultured using Dulbecco's Modified Eagle's Medium + 10% fetal bovine serum + 1 μL/mL of Pen-Strep antibiotic. A431-CD cells were exposed to a 2 μM solution of cytochalasin D (Sigma-Aldrich, St. Louis, MO) for 30 min before imaging. A549 lung cancer cells were cultured using Dulbecco's Modified Eagle's Medium + 10% fetal bovine

serum + 1 μL/mL of Pen-Strep antibiotic. Cells were obtained from the Duke Cell Culture Facility, which performed STR authentication and mycoplasma contamination testing of all cell lines used. Cells were plated onto 40 mm No. 1 coverslips at low density and were allowed to attach overnight. The following day, the coverslips were inserted into a flow cell (Bioptechs FCS3, Butler, PA) with a flow cell width of 14 mm and a channel height of 0.25 mm, and were immediately analyzed.

RESULTS

QPI provides disorder strength

To assess the morphological heterogeneity of the cells under investigation, we devised a new method for measuring disorder strength using QPI by analyzing the local variance of phase across the cell. In this analysis, the cell is treated as a thin, weakly scattering and absorbing object, which induces a phase delay, $\varphi(x,y)$, according to

$$\varphi(x, y) = \frac{2\pi}{\lambda}\Delta n(x, y)d(x, y), \tag{3}$$

where $d(x,y)$ is the axial height of the cell at point (x, y), λ is the wavelength of illumination, and Δn refers to the RI difference between the cell, $n_{cell}(x,y)$, and the surrounding media, n_{media}. The fluctuations in RI, Δn, can be viewed as representing the distribution of intracellular solids (42). For a given point (x,y) within the apical portion of the cell, we can assume $d(x,y)$ does not vary greatly across the local region and treat it as a constant. Thus, the variance of the phase in a given 3×3-pixel region is directly proportional to the variance of the cell RI, $\langle\Delta\varphi(x, y)^2\rangle \propto \langle\Delta n(x, y)^2\rangle$, related by the square of the wavenumber and the square of the axial height. This relationship would require knowledge of the cell height to determine the refractive index variance from the phase variance data. To avoid this uncertainty, the phase variance is normalized by the square mean phase in the corresponding 3×3 window, $\overline{\varphi}^2$, to create a phase fluctuation metric, $\langle\Delta\varphi(x, y)^2\rangle/\overline{\varphi}^2(x, y)$ (see Fig. 2). This form does not depend on the axial height. Multiplying the phase fluctuation metric by the square of the average cellular RI, $\overline{n}^2$, consequently yields the spatial variance of the cellular RI $\langle\Delta n(x, y)^2\rangle$, such that:

$$\frac{\langle\Delta\varphi(x, y)^2\rangle}{\overline{\varphi}^2(x, y)} \approx \frac{\langle\Delta n(x, y)^2\rangle}{\overline{n}^2}, \tag{4}$$
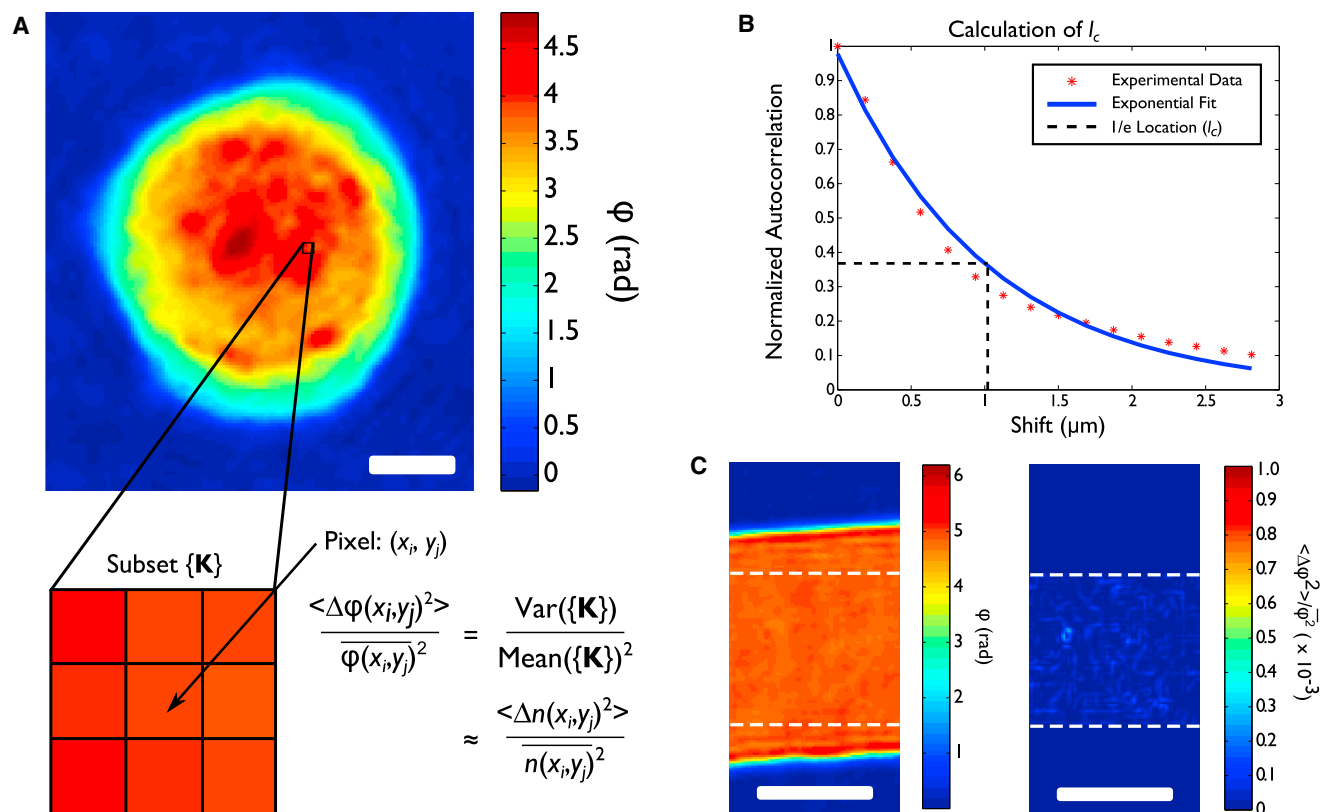

FIGURE 2 Calculation of disorder strength, L_D. (A) Example phase image of an HT-29 cell. Phase fluctuations at a given point (x_i, y_j) were calculated by analyzing the 3×3-pixel neighborhood, **K,** surrounding the given point. Dividing the variance by the mean squared phase of this local 3×3 neighborhood at **K** gives phase fluctuation that is related to RI fluctuations, as shown (scale bar = 10 μm). (B) Calculation of l_c: example autocorrelation calculation showing the exponential falloff and subsequent fitting to retrieve spatial correlation length parameter, l_c. (C) Example phase image (left) of a thin PDMS slab showing a steady phase value (scale bar = 10 μm). The phase fluctuations, calculated in the region delineated by white dashed lines (right), show very few changes. To see this figure in color, go online.

with an illustration describing this method shown in Fig. 2.

The disorder strength is defined as $L_D = \langle \Delta n^2 \rangle l_c$, where l_c is the spatial coherence length, which describes the characteristic size of cell structures. In these experiments, l_c was determined experimentally for each cell by calculating the autocorrelation of the phase fluctuation image and fitting the falloff to an exponential form (Fig. 2 B). This enables calculation of disorder strength as:

$$L_D = \left\langle \frac{\langle \Delta\varphi(x,y)^2 \rangle}{\overline{\varphi}^2(x,y)} \right\rangle \overline{n}^2 l_c. \qquad (5)$$

Here, the $\langle \ldots \rangle$ notation indicates a statistical average across the 3×3-pixel neighborhood in x and y while the overbar notation refers to the average value across this region. The phase fluctuation image of a cell, $\langle \Delta\varphi(x,y)^2 \rangle / \overline{\varphi}^2(x,y)$, is also averaged across a given cell or region to yield a single disorder strength value. While this metric is very similar to disorder strength as calculated by Subramanian et al. (33), there are important differences to note. First, Eq. 5 describes disorder strength of RI variations across a 3×3-pixel spatial window, whereas the form used by Subramanian et al. (33) refers to RI variations within a single axial volume (i.e., a pixel). Second, we can directly calculate the correlation length from our phase images, which is delineated by our diffraction-limited resolution. In contrast, Subramanian et al. (33) determine L_D from spectral data and do not obtain separate knowledge of coherence length or RI fluctuations (35). To show a typical calculation, the disorder strength was calculated for a control sample, shown in Fig. 2. The phase data in Fig. 2 C show a flat background field (blue) with an area of increased phase (orange), where a segment of PDMS is located. The PDMS segment shows low disorder, as expected for this uniform material. However, some small, nonzero values of disorder are seen, suggesting inhomogeneities within the segment. Further measurements of control samples with defined properties are presented in the Supporting Material. We note that the observed phase variations are significantly larger than the phase noise of the system. The spatial phase noise variance of the system was 6.4×10^{-5} rad^2, and measured cell variances were on the order of 1×10^{-3} to 1×10^{-2} rad^2. Therefore, phase noise is not expected to have a significant impact on the measurements.

Disorder strength across cancer cell lines

To evaluate the utility of phase-based disorder strength measurements, differences in L_D were examined for two different cell populations, HT-29 colon cancer cells and HT-29 cells with a CSK shRNA-mediated knock-down. These two cell lines cells were previously analyzed for disorder strength using partial wave spectroscopy (PWS) with

the transformed line found to have a 30–50% decrease in expression of CSK and increased epithelial cellular proliferation, malignant aggressiveness, and cytoskeletal dysregulation (32,33). Significantly, while HT-29 cells and their CSK knockdown counterpart were not readily distinguished by a pathologist using standard imaging techniques, CSK cells were found to have increased disorder strength compared to the nontransfected HT-29 cells (32,33). This cell system provides two nearly identical cell populations with subtle cytoskeletal differences that might be expected to translate into changes in cellular stiffness. CSK cells are also expected to exhibit decreased cellular stiffness given their increased metastatic potential, which is usually associated with dysregulation of the cytoskeleton (9–14,43).

The disorder strength is calculated directly from individual cell images, providing a large number of measurements in as little time as it takes to reposition new fields of view of the cell sample. For these experiments, quantitative phase measurements were conducted on ~40 cells randomly selected from the two cell types. To compare similar areas of the cell, only regions of the cell where $\varphi(x,y) > 2.75$ rad were analyzed, which also served to avoid artifacts induced by the large spatial gradient at the cell periphery, where the assumption of slowly varying axial cell height is not valid (see Materials and Methods for discussion on selection of threshold). Using this threshold, the average areas of interrogation for HT-29 and CSK cells, respectively, were $5.57 \pm 1.91 \times 10^3$ and $5.59 \pm 1.51 \times 10^3$ pixels, resulting in a statistically similar area of investigation ($p > 0.58$, two-sided Wilcoxon rank-sum). The phase fluctuation metric, $\langle \Delta\varphi(x,y)^2 \rangle / \overline{\varphi}^2(x,y)$, was calculated for each pixel of interest in each cell and whole-cell values of L_D were determined by taking the mean value of the log-normal distribution and applying Eq. 5. The mean cellular RI was assumed to be $\overline{n} = 1.38$.

Example phase images of HT-29 and CSK cells can be seen in Fig. 3. Fig. 3, A and C, shows example QPI images of these two cell types. Both images show a rapid increase in phase at the periphery of the cell, and a slowly varying phase change across the cell apex. Fig. 3, B and D, shows example phase fluctuation images of the HT-29 and CSK cells, shown in Fig. 3, A and C, respectively, with the same scale bar. As can be seen in this example, the magnitude of the phase fluctuations is much higher for the CSK cell. Furthermore, this increased phase fluctuation appears throughout the CSK cell, whereas the HT-29 cell shows fewer and more sparse fluctuations. The probability density functions of the phase fluctuations of the two example cells (Fig. 3, B and D) can be seen in Fig. 3 K. The two distributions appear log-normal; in addition, the CSK distribution is noticeably skewed compared to the HT-29 distribution, leading to a larger mean value of $\langle \Delta\varphi(x,y)^2 \rangle / \overline{\varphi}^2(x,y)$ for the CSK cell-line.

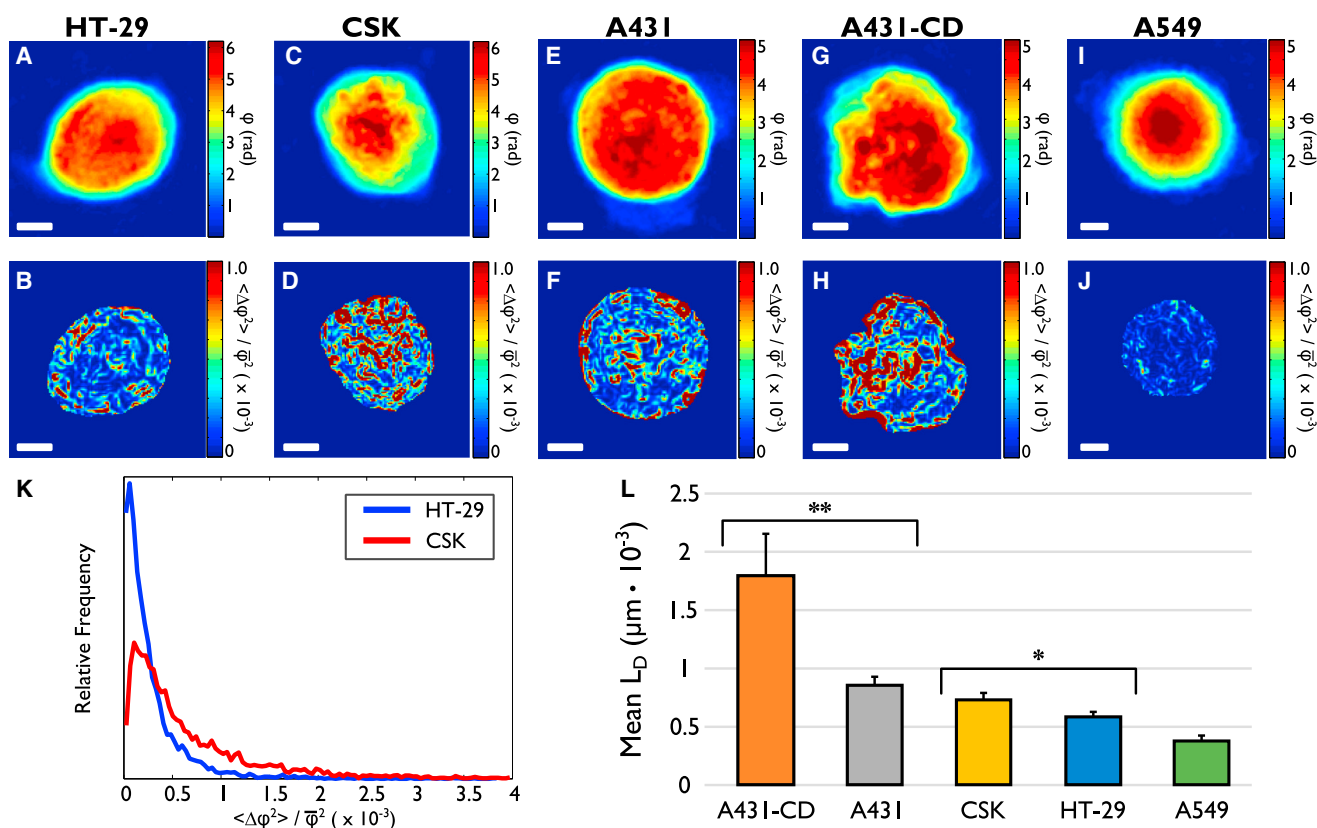Fig. 3 L compares the disorder strength across the two populations. CSK cells ($N = 39$) were found to have

FIGURE 3   Disorder strength varies among cell lines. Example phase and phase fluctuation images, for (*A* and *B*) HT-29 (*N* = 37), (*C* and *D*) CSK (*N* = 39), (*E* and *F*) A431 (*N* = 22), (*G* and *H*) A431-CD (*N* = 22), and (*I* and *J*) A549 cell lines (*N* = 27). All scale bars are 5 μm. (*K*) Frequency histogram of the phase fluctuations of images shown in (*B*) and (*D*). Distributions appear log-normal and are right skewed for CSK cells. (*L*) Mean disorder strength for the five cell populations tested (mean ± SE as error bars). A431-CD cells were significantly more disordered than their normal A431 counterparts. CSK cells were also significantly more disordered than HT-29 cells. A549 cells had the lowest mean disorder strength of all populations tested. *P* values were calculated using a two-sided Wilcoxon rank-sum test. *P < 0.002; **P < 0.0003. To see this figure in color, go online.

significantly higher ($p < 0.002$, two-sided Wilcoxon rank-sum) phase disorder strengths than the HT-29 cells (*N* = 37). CSK cells had a group average (mean ± SE) L_D of $7.34 \times 10^{-4} \pm 0.43 \times 10^{-4}$ μm, while HT-29 cells had a mean L_D of $5.87 \times 10^{-4} \pm 0.32 \times 10^{-4}$ μm. This result is in agreement with previous results using PWS, which found that CSK cells had larger disorder strengths than unmodified HT-29 cells (32,33).

To investigate disorder strength further, we sought to examine additional cell lines with varying mechanical properties. Previously, we studied the mechanical properties of A431 skin cancer cells and A431 cells exposed to cytochalasin D (i.e., A431-CD) (19). Normal A431 cells are expected to have similar disorder strengths as both populations of HT-29 cells, given the similarity in stiffness, cell shape, base area, and substrate attachment. However, A431-CD cells are expected to have much higher disorder strengths due to the disruption of the cytoskeleton. Example phase images and phase fluctuation images of A431 and A431-CD cells can be seen in Fig. 3, *E* and *F*, and *G* and *H*, respectively. A431 cells (*N* = 22) had an average L_D of $8.58 \times 10^{-4} \pm 0.72 \times 10^{-4}$ μm, while A431-CD cells (*N* = 22)

had a mean L_D of $17.99 \times 10^{-4} \pm 3.64 \times 10^{-4}$ μm, a significantly higher disorder strength compared to the untreated A431 cells ($p < 3 \times 10^{-4}$, two-sided Wilcoxon rank-sum). The influence of the cytoskeleton on the overall disorder strength was examined by calculating the disorder of fluorescently stained actin in confocal images (see the Supporting Material). These measurements show that the trend in disorder strength was preserved within cell lines (HT-29 versus CSK and A431 versus A431 CD) but not across cell lines. The relationship between the total L_D values and those from the fluorescence images are discussed below. As a final example, A549 cells were also examined (Fig. 3, *I* and *J*). These cells have a larger spread of attachment and thus were expected to exhibit a lower mean disorder strength. Indeed, A549 cells (*N* = 27) had a group mean L_D of $3.81 \times 10^{-4} \pm 0.40 \times 10^{-4}$ μm, the lowest of any of the cells examined in this study.

Disorder strength is linked to cell stiffness

It is hypothesized that shear stiffness is negatively correlated with disorder strength, as cells with increased structural

disorder (and thus disorder strength) are expected to offer less resistance to extracellular stress. To compare disorder strength to the effective shear stiffness, k_s, each cell line was also evaluated using our shear stress flow assay. In this assay, phase images are acquired over an 8 s period after application of a step change in shear flow. The center of mass displacement is calculated for each image and the trend versus time was fit using a 1D Kelvin-Voigt viscoelastic model to determine shear stiffness as described in Eldridge et al. (19). Briefly, the effective force on the cell is determined from the shear stress and the projected cellular surface area, also determined from the phase imaging data. Using this phase measurement of displacement and effective force, the 1D Kelvin-Voigt viscoelastic model can be used to fit the data, producing a determination of the effective shear stiffness constant, k_s.

The initial comparison between HT-29 and CSK cells sought to confirm differences in their mechanical properties. Steady-state phase displacements for the two cell groups after being subjected to 8 s (i.e., $\varphi(x,y, T = 8 \text{ s})$ − $\varphi(x,y, T = 0 \text{ s})$) of shear flow at a shear stress of 8 dyne/cm² may be seen in Fig. 4, A and B. While the two cell lines still experience some dynamic displacement after 8 s, the majority of the COM movement occurs before this time. Fig. 4 A shows a very homogenous displacement, likely due to the lack of RI variations within the cell, especially across the apical portion. However, Fig. 4 B shows a more disorganized displacement profile for the CSK cell.

Unlike the HT-29 cell, there appears to be clusters of significant mass displacements in the center of the cell, likely due to high RI components, which have been mechanically displaced due to the applied stress. The CSK group had an average stiffness (mean ± SE) of 0.86 ± 0.09 mN/m, while HT-29 cells had a group mean stiffness of 1.40 ± 0.13 mN/m. The projected surface areas between the two cells was found to be statistically similar (CSK: 830 ± 190 μm^2; HT-29: 851 ± 224 μm^2; $p > 0.65$, two-sided Wilcoxon rank-sum), confirming that surface area differences between the two cells would not confound shear stiffness measurements (see Materials and Methods for detailed description of impact of surface area on shear stiffness calculations). CSK cells were found to have significantly lower k_s values than HT-29 cells ($p < 3 \times 10^{-4}$, two-sided Wilcoxon rank-sum) as seen in Fig. 4 F. As expected, CSK cells were less stiff and more disordered than their genetically unaltered HT-29 equivalents. Videos of cell phase displacements over the course of the shear stimulus for both HT-29 and CSK cells may be found in the Supporting Material.

The other cell lines in this study captured a wide range of mechanical properties. The A431 cells were similar to the CSK cells, producing an effective shear stiffness value of 0.93 ± 0.09 mN/m. In contrast, the A431-CD cells exhibited a significantly lower ($p < 5 \times 10^{-6}$, two-sided Wilcoxon rank-sum) mean stiffness value of 0.42 ± 0.04 mN/m. The A549 cells had a higher stiffness that any
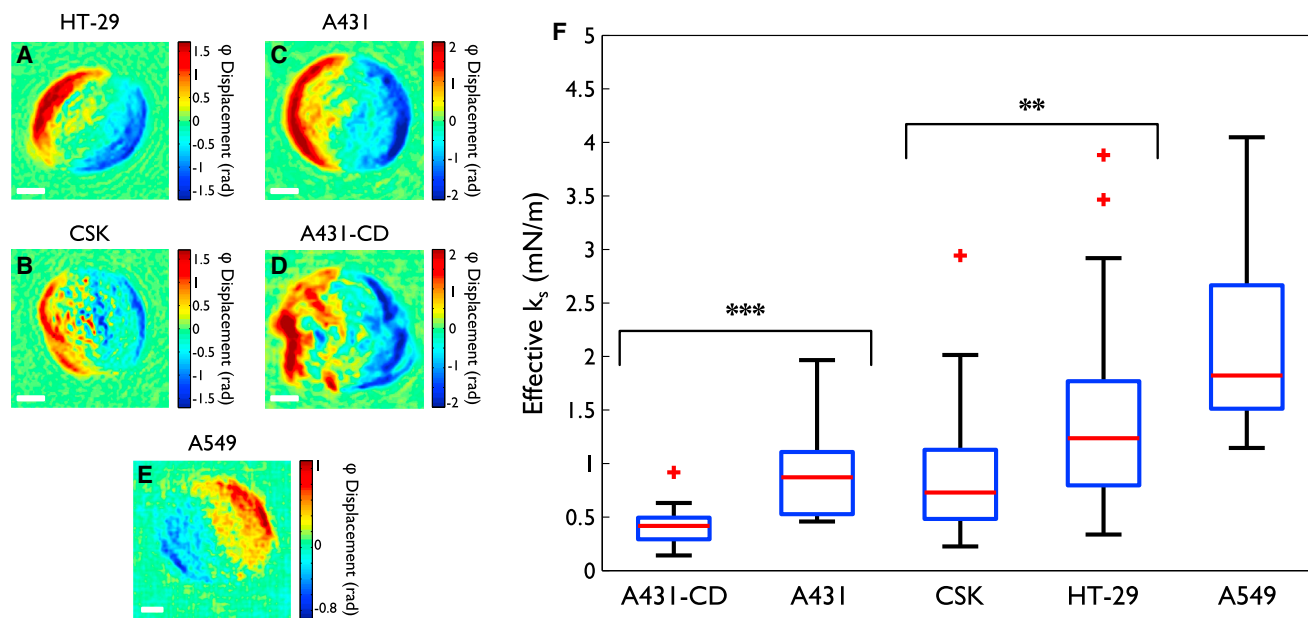

FIGURE 4 Stiffness profiles of interrogated cell lines. Phase displacement images after being subjected to 8 s of shear stress for (A) HT-29 (N = 37), (B) CSK (N = 39), (C) A431 (N = 22), (D) A431-CD (N = 22), and (E) A549 (N = 27) cells. Note that these displacements, corresponding to the same cells shown in Fig. 3, are given in radians. (F) Effective k_s distributions for all five populations tested. A431-CD cells were significantly more compliant than their normal A431 counterparts. CSK cells were also significantly less stiff than HT-29 cells. As expected, A549 cells exhibited the stiffest profile of all cell types tested. Box plot represents the range of k_s values measured, with the red line corresponding to the median, the blue box referring to the interquartile distribution, and the red plus-signs signifying outliers. P values were calculated using a two-sided Wilcoxon rank-sum test. **$P < 0.0003$; ***$P < 5 \times 10^{-6}$. To see this figure in color, go online.

of the other cell lines examined here of k_s of 2.16 ± 0.16 mN/m. These results are summarized in Fig. 4.

We now consider the relationship between phase disorder strength and cellular stiffness. A clear connection between L_D and k_s was observed, as cells that were on average twice as compliant (A431-CD) were on average twice as disordered. Further, A431 cells had a stiffness and disorder strength profile that seemed to classify them as more similar to CSK and HT-29 cells as they had a similar profile to CSK cells in stiffness ($p > 0.34$, two-sided Wilcoxon rank-sum), and were more similar to CSK cells in terms of phase disorder strength ($p > 0.11$, two-sided Wilcoxon rank-sum). In line with our hypothesis, A549 cells had significantly lower phase disorder strength and significantly higher effective shear stiffness as compared to HT-29 cells ($p < 1 \times 10^{-4}$, two-sided Wilcoxon rank-sum). Most interestingly, a noticeable trend is seen when plotting mean L_D versus mean k_s for the five cell populations studied (Fig. 5). An inverse relationship between L_D and k_s was found to exist between the five cell types, with a substantial coefficient of determination ($r^2 = 0.978$) pointing to good agreement between the model and the data. The constant parameter, b, which links L_D and k_s in the model, was found to be 0.75 pN. Interestingly, this value is on the same order as the force of typical cell processes such as a single actin filament polymerization (44) or the interaction force between myosin and actin (45).

As described in the Materials and Methods, the determination of phase disorder strength is based on a single image acquisition. Therefore, with disorder strength presenting a clear relationship to cellular stiffness (i.e., higher average L_D means lower average k_s), estimations of cellular mechanical properties can be evaluated and predicted without having to mechanically perturb the cell, as is done in our shear

stiffness assay and every other microrheological technique to our knowledge. The implications of this relationship are discussed below.

DISCUSSION

QPI provides a fast and robust way of analyzing weak RI inhomogeneity via its subnanometer sensitivity to optical path length changes, providing a unique tool for characterizing cell structures. Here, we have demonstrated the ability of QPI to detect nanoscale fluctuations of RI in a range of cellular systems using the theoretical framework of disorder strength, L_D. Specifically, QPI measurements of disorder strength were able to discriminate between two similar cell populations, HT-29 colon cancer cells and their CSK knockdown variant. Confirming previous findings, QPI verified that the more malignant aggressive CSK cells have higher disorder strength than the less aggressive HT-29 cells. These measurements are slightly higher by a similar factor (~2–3×) than those presented by Damania et al. (32) for CSK cells ($L_D \approx 4.5 \times 10^{-4}$ μm) and HT-29 cells ($L_D \approx 2 \times 10^{-4}$ μm), but this earlier work examined fixed cells while measurements for live cells are presented here. The shear stiffness assay we previously developed using QPI (19) was employed to connect measurements of disorder strength to the mechanical properties of the two cell lines. Due to the subtle cytoskeletal differences between the two that drives the difference in disorder strength (32), it was also verified that the less proliferative HT-29 cell line was significantly more stiff than the higher metastatic potential CSK cells. These results demonstrate that QPI can be used to not only differentiate the two cell lines by quantifying differences in whole-cell mechanical properties, but also by differences in cellular nanoarchitecture. We were able to identify an inverse relationship between L_D and k_s by expanding the study to examine more cell lines with varied mechanical properties. Previously analyzed A431 cells, and A431 cells disrupted with cytochalasin D, provided a means to compare two cell lines with known differences in mechanical properties as the A431 cells were much stiffer and much less disordered than A431-CD, reinforcing the correlation between disorder strength and mechanical stiffness. With the inclusion of a third distinct cell line (A549 lung cancer cells) that had differing mechanical properties, a profound relationship was established between disorder strength and the effective whole cell shear stiffness. As seen in Fig. 5, a strong inverse relationship ($r^2 = 0.978$) was discovered between the averages of the two QPI-derived metrics for each population.

Fig. 6 illustrates the possible mechanism between the two cell attributes. Disorder strength represents the organization of subcellular structures, but here for illustration purposes, we focus on cytoskeletal arrangement. As shown by Gupta et al. (18), cells with varying degrees of cytoskeletal order exhibit differing ability to generate traction forces, an aspect
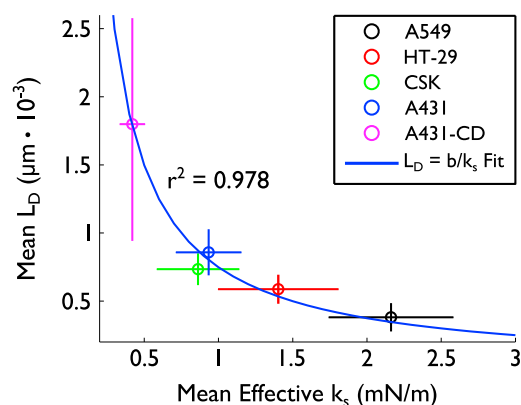

FIGURE 5 Negative correlation between L_D and k_s. Mean effective shear stiffness, k_s, versus mean phase disorder strength, L_D, in five different cell populations. The width of the error bars corresponds to the standard deviation in each dimension. An inverse relationship between L_D and k_s appears to exist (fit parameters: $b = 7.5 \times 10^{-4}$ nN, $r^2 = 0.978$). To see this figure in color, go online.
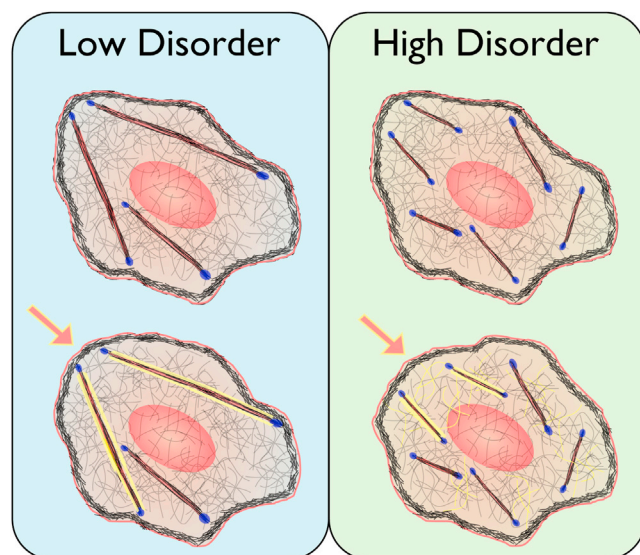
FIGURE 6 Theoretical mechanism connecting disorder and stiffness. (*Left*) Cell with well-ordered cytoskeleton enables more efficient force transfer and provides greater resistance to applied stress (*arrow*). (*Right*) Cell with a disordered cytoskeleton causes distributed transfer of force, resulting in greater reorganization of cell components in response to applied stress (*arrow*), resulting in lower resistance. To see this figure in color, go online.

of their mechanical properties. Cells with greater order, shown on the left in Fig. 6, enable more efficient transfer of mechanical forces, resulting in greater stiffness. In contrast, cells with disordered cytoskeletal arrangements permit a more distributed stress transfer (Fig. 6, *right*), allowing for significant rearrangement of mass density in response to applied force and a greater deformation for a given force. This trend is seen in the transformed cells used in this study. The CSK cells have a more disorganized cytoskeleton than the HT-29 cells and are seen to be more compliant. In the extreme case of the A431-CD cells, the actin cytoskeleton is severely disrupted (46,47), as confirmed with the sharp increase in disorder strength, resulting in a highly compliant cell, as indicated by the low stiffness measurements. Based on our measurements of the disorder strength for the whole cell and those for cytoskeletal disorder shown in the Supporting Material, it can be seen that there is a relationship between the two but the cytoskeleton organization is not solely responsible for cell mechanical properties as seen in the trends observed here.

These results point to a relationship that may have implications in cellular mechanobiology. Given the clear relationship between the two metrics, high throughput cell studies can be used to assess cell mechanical properties based solely on RI inhomogeneity (i.e., disorder strength). Alterations in cellular stiffness and cytoskeletal organization, as mentioned earlier, have been shown to be a precursor to oncogenesis and play an important role in metastasis (10,12–14,43). Despite the importance of these mechanical differences for both understanding disease etiology and discriminating cell phenotype, the cellular stiffness or elasticity has yet to become a significant diagnostic approach because differences can only be measured precisely using cumbersome and slow methods like atomic force microscopy, optical tweezers, and micropipette aspiration. Furthermore, while other high throughput cellular rheological techniques have been proposed as a means to differentiate normal and cancerous cells via deformability, they have yet to provide a suitable modality for diagnosis because they lack the precision to discern stiffness differences between cancers of different metastatic potential (48–51). Therefore, having a single-acquisition, noncontact technique like QPI that can make inferences on mechanical status without the need to apply stress to the object of interest, could have a significant role in high throughput studies of cancer cellular mechanics. While it may not be true that all cell types will follow a universal inverse relationship as shown here, it is possible that particular cell types may present their own unique $L_D - k_s$ curve, which could be used to monitor relative aggressiveness of a particular genotype (e.g., HT-29 versus CSK) in a particular cancer type. Further studies are needed to better define the underlying mechanism between the two metrics. Differences in cytoskeletal organization clearly have an influence on mechanical cell properties, which can be seen in the disorder strength differences between the transformed cell lines examined here. However, the cytoskeleton organization is not solely responsible for the observed trends in both increased disorder strength and decreased mechanical stiffness because measurements of cytoskeleton disorder (shown in the Supporting Material) only partly explain them. Future studies with technical samples of known disorder strength (i.e., self-assembled nanosphere lattices) and cell studies that dissect the contribution of specific structures to overall cell properties will more clearly illuminate the relationship between these two attributes.

In conclusion, we have demonstrated a new method for determining cell disorder strength. The simplicity of the QPI setup and straightforward analysis suggest that this approach could readily be implemented in a high throughput scheme to generate large-volume studies of cellular morphology. The QPI platform is also the basis of a shear flow assay for measuring cell stiffness, providing a simple means of comparing these two aspects of cell phenotype. By examining a range of cell populations, we established a relationship between cell disorder strength and mechanical stiffness. This relationship can be exploited to predict mechanical properties based on disorder strength measurements, a useful capacity for a range of applications. However, the existence of the relationship also suggests that the overall organization of structures in the cell is responsible for its mechanical stiffness.

SUPPORTING MATERIAL

Supporting Materials and Methods, two figures, and two movies are available at http://www.biophysj.org/biophysj/supplemental/S0006-3495(16)34319-3.

AUTHOR CONTRIBUTIONS

A.W. and W.J.E wrote the main article text; W.J.E., Z.A.S., and B.L. prepared samples, conducted imaging experiments, and analysis; Z.A.S. and B.L. contributed to article revisions; and A.W. and W.J.E. conceived experimental design and methods of analysis.

ACKNOWLEDGMENTS

REFERENCES

1. Bao, G., and S. Suresh. 2003. Cell and molecular mechanics of biological materials. *Nat. Mater.* 2:715–725.

2. Suresh, S. 2007. Biomechanics and biophysics of cancer cells. *Acta Biomater.* 3:413–438.

3. Blanchoin, L., R. Boujemaa-Paterski, …, J. Plastino. 2014. Actin dynamics, architecture, and mechanics in cell motility. *Physiol. Rev.* 94:235–263.

4. Clark, A. G., and E. Paluch. 2011. Mechanics and regulation of cell shape during the cell cycle. *Results Probl. Cell Differ.* 53:31–73.

5. Azeloglu, E. U., J. Bhattacharya, and K. D. Costa. 2008. Atomic force microscope elastography reveals phenotypic differences in alveolar cell stiffness. *J. Appl. Physiol.* 105:652–661.

6. Docheva, D., D. Padula, …, M. Schieker. 2008. Researching into the cellular shape, volume and elasticity of mesenchymal stem cells, osteoblasts and osteosarcoma cells by atomic force microscopy. *J. Cell. Mol. Med.* 12:537–552.

7. McGrail, D. J., R. Mezencev, …, M. R. Dawson. 2015. SNAIL-induced epithelial-to-mesenchymal transition produces concerted biophysical changes from altered cytoskeletal gene expression. *FASEB J.* 29:1280–1289.

8. Liu, J., N. Sun, …, M. J. Butte. 2012. Atomic force mechanobiology of pluripotent stem cell-derived cardiomyocytes. *PLoS One.* 7:e37559.

9. Xinyi, G., B. Keith, …, G. Martin. 2014. The effect of neighboring cells on the stiffness of cancerous and non-cancerous human mammary epithelial cells. *New J. Phys.* 16:105002.

10. Cross, S. E., Y. S. Jin, …, J. K. Gimzewski. 2007. Nanomechanical analysis of cells from cancer patients. *Nat. Nanotechnol.* 2:780–783.

11. Rother, J., H. Nöding, …, A. Janshoff. 2014. Atomic force microscopy-based microrheology reveals significant differences in the viscoelastic response between malign and benign cell lines. *Open Biol.* 4:140046.

12. Fife, C. M., J. A. McCarroll, and M. Kavallaris. 2014. Movers and shakers: cell cytoskeleton in cancer metastasis. *Br. J. Pharmacol.* 171:5507–5523.

13. Yamaguchi, H., and J. Condeelis. 2007. Regulation of the actin cytoskeleton in cancer cell migration and invasion. *Biochim. Biophys. Acta.* 1773:642–652.

14. Olson, M. F., and E. Sahai. 2009. The actin cytoskeleton in cancer cell motility. *Clin. Exp. Metastasis.* 26:273–287.

15. Kuznetsova, T. G., M. N. Starodubtseva, …, R. I. Zhdanov. 2007. Atomic force microscopy probing of cell elasticity. *Micron.* 38:824–833.

16. Nawaz, S., P. Sánchez, …, I. A. Schaap. 2012. Cell visco-elasticity measured with AFM and optical trapping at sub-micrometer deformations. *PLoS One.* 7:e45297.

17. Tsai, M. A., R. S. Frank, and R. E. Waugh. 1993. Passive mechanical behavior of human neutrophils: power-law fluid. *Biophys. J.* 65:2078–2088.

18. Gupta, M., B. R. Sarangi, …, B. Ladoux. 2015. Adaptive rheology and ordering of cell cytoskeleton govern matrix rigidity sensing. *Nat. Commun.* 6:7525.

19. Eldridge, W. J., A. Sheinfeld, …, A. Wax. 2016. Imaging deformation of adherent cells due to shear stress using quantitative phase imaging. *Opt. Lett.* 41:352–355.

20. Jourdain, P., D. Boss, …, P. Marquet. 2012. Simultaneous optical recording in multiple cells by digital holographic microscopy of chloride current associated to activation of the ligand-gated chloride channel GABA$_A$ receptor. *PLoS One.* 7:e51041.

21. Pavillon, N., J. Kühn, …, P. Marquet. 2012. Early cell death detection with digital holographic microscopy. *PLoS One.* 7:e30912.

22. Shaked, N. T., J. D. Finan, …, A. Wax. 2010. Quantitative phase microscopy of articular chondrocyte dynamics by wide-field digital interferometry. *J. Biomed. Opt.* 15:010505.

23. Shaked, N. T., L. L. Satterwhite, …, A. Wax. 2010. Whole-cell-analysis of live cardiomyocytes using wide-field interferometric phase microscopy. *Biomed. Opt. Express.* 1:706–719.

24. Byun, H., T. R. Hillman, …, Y. Park. 2012. Optical measurement of biomechanical properties of individual erythrocytes from a sickle cell patient. *Acta Biomater.* 8:4130–4138.

25. Park, Y., C. A. Best, …, G. Popescu. 2010. Measurement of red blood cell mechanics during morphological changes. *Proc. Natl. Acad. Sci. USA.* 107:6731–6736.

26. Park, Y., M. Diez-Silva, …, S. Suresh. 2008. Refractive index maps and membrane dynamics of human red blood cells parasitized by *Plasmodium falciparum. Proc. Natl. Acad. Sci. USA.* 105:13730–13735.

27. Shaked, N. T., L. L. Satterwhite, …, A. Wax. 2011. Quantitative microscopy and nanoscopy of sickle red blood cells performed by wide field digital interferometry. *J. Biomed. Opt.* 16:030506.

28. Willig, K. I., B. Harke, …, S. W. Hell. 2007. STED microscopy with continuous wave beams. *Nat. Methods.* 4:915–918.

29. Willig, K. I., S. O. Rizzoli, …, S. W. Hell. 2006. STED microscopy reveals that synaptotagmin remains clustered after synaptic vesicle exocytosis. *Nature.* 440:935–939.

30. Betzig, E., G. H. Patterson, …, H. F. Hess. 2006. Imaging intracellular fluorescent proteins at nanometer resolution. *Science.* 313:1642–1645.

31. Shroff, H., C. G. Galbraith, …, E. Betzig. 2008. Live-cell photoactivated localization microscopy of nanoscale adhesion dynamics. *Nat. Methods.* 5:417–423.

32. Damania, D., H. Subramanian, …, V. Backman. 2010. Role of cytoskeleton in controlling the disorder strength of cellular nanoscale architecture. *Biophys. J.* 99:989–996.

33. Subramanian, H., P. Pradhan, …, V. Backman. 2008. Optical methodology for detecting histologically unapparent nanoscale consequences of genetic alterations in biological cells. *Proc. Natl. Acad. Sci. USA.* 105:20118–20123.

34. Damania, D., H. K. Roy, …, V. Backman. 2012. Nanocytology of rectal colonocytes to assess risk of colon cancer based on field cancerization. *Cancer Res.* 72:2720–2727.

35. Subramanian, H., P. Pradhan, …, V. Backman. 2009. Partial-wave microscopic spectroscopy detects subwavelength refractive index fluctuations: an application to cancer diagnosis. *Opt. Lett.* 34:518–520.

36. Subramanian, H., H. K. Roy, …, V. Backman. 2009. Nanoscale cellular changes in field carcinogenesis detected by partial wave spectroscopy. *Cancer Res.* 69:5357–5363.

37. Rinehart, M., Y. Zhu, and A. Wax. 2012. Quantitative phase spectroscopy. *Biomed. Opt. Express.* 3:958–965.

38. Akcay, C., P. Parrein, and J. P. Rolland. 2002. Estimation of longitudinal resolution in optical coherence imaging. *Appl. Opt.* 41:5256–5262.

39. Rinehart, M. T., H. S. Park, and A. Wax. 2015. Influence of defocus on quantitative analysis of microscopic objects and individual cells with digital holography. *Biomed. Opt. Express.* 6:2067–2075.

40. Mathur, A. B., W. M. Reichert, and G. A. Truskey. 2007. Flow and high affinity binding affect the elastic modulus of the nucleus, cell body and the stress fibers of endothelial cells. *Ann. Biomed. Eng.* 35:1120–1130.

41. Cornish, R. J. 1928. Flow in a pipe of rectangular cross-section. *Proc. Roy. Soc. Lond. A Mat.* 120:691–700.

42. Barer, R. 1952. Interference microscopy and mass determination. *Nature.* 169:366–367.

43. Hall, A. 2009. The cytoskeleton and cancer. *Cancer Metastasis Rev.* 28:5–14.

44. Kovar, D. R., and T. D. Pollard. 2004. Insertional assembly of actin filament barbed ends in association with formins produces picoNewton forces. *Proc. Natl. Acad. Sci. USA.* 101:14725–14730.

45. Laakso, J. M., J. H. Lewis, …, E. M. Ostap. 2008. Myosin I can act as a molecular force sensor. *Science.* 321:133–136.

46. Wakatsuki, T., B. Schwab, …, E. L. Elson. 2001. Effects of cytochalasin D and latrunculin B on mechanical properties of cells. *J. Cell Sci.* 114:1025–1036.

47. Petersen, N. O., W. B. McConnaughey, and E. L. Elson. 1982. Dependence of locally measured cellular deformability on position on the cell, temperature, and cytochalasin B. *Proc. Natl. Acad. Sci. USA.* 79:5327–5331.

48. Dudani, J. S., D. R. Gossett, …, D. Di Carlo. 2013. Pinched-flow hydrodynamic stretching of single-cells. *Lab Chip.* 13:3728–3734.

49. Gossett, D. R., H. T. K. Tse, …, D. Di Carlo. 2012. Hydrodynamic stretching of single cells for large population mechanical phenotyping. *Proc. Natl. Acad. Sci. USA.* 109:7630–7635.

50. Tse, H. T. K., D. R. Gossett, …, D. Di Carlo. 2013. Quantitative diagnosis of malignant pleural effusions by single-cell mechanophenotyping. *Sci. Transl. Med.* 5:212ra163.

51. Guck, J., R. Ananthakrishnan, …, J. Käs. 2001. The optical stretcher: a novel laser tool to micromanipulate cells. *Biophys. J.* 81:767–784.